An ultrasensitive FET biosensor based on vertically aligned MoS$_2$ nanolayers with abundant surface active sites

Pengfei Song [a,b,c], Pengfei Ou [d], Yongjie Wang [e], Hang Yuan [c], Sixuan Duan [c], Longyan Chen [f], Hao Fu [a,b], Jun Song [b], Xinyu Liu [a,*]

[a] Department of Mechanical and Industrial Engineering, University of Toronto, 5 King's College Road, Toronto, Ontario, M5S 3G8, Canada
[b] Department of Mechanical Engineering, McGill University, 817 Sherbrooke Street West, Montreal, Quebec, H3A 0C3, Canada
[c] School of Advanced Technology, Xi'an Jiaotong-Liverpool University, 111 Ren'ai Road, Suzhou, 215000, China
[d] Department of Mining and Materials Engineering, McGill University, 3610 Rue University, Montreal, Quebec, H3A 0C5, Canada
[e] School of Science, Harbin Institute of Technology-Shenzhen, 1 Pingshan Road, Shenzhen, 518000, China
[f] Department of Biomedical, Industrial & Systems Engineering, Gannon University, 109 University Square, Erie, PA, 16541, USA

HIGHLIGHTS

- Chemical vapor deposition grew vertically-aligned MoS$_2$ nanolayers.
- Vertically-aligned MoS$_2$ nanolayers facilitate molecule functionalization.
- A field-effect transistor based on vertically-aligned MoS$_2$ nanolayers was built.
- It shows ultra-sensitivity for prostate-specific antigen detection in human serum.

GRAPHICAL ABSTRACT
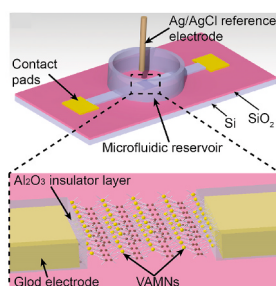
ARTICLE INFO

ABSTRACT

Molybdenum disulfide (MoS$_2$) nanolayers are one of the most promising two-dimensional (2D) nanomaterials for constructing next-generation field-effect transistor (FET) biosensors. In this article, we report an ultrasensitive FET biosensor that integrates a novel format of 2D MoS$_2$, vertically-aligned MoS$_2$ nanolayers (VAMNs), as the channel material for label-free detection of the prostate-specific antigen (PSA). The developed VAMNs-based FET biosensor shows two distinctive advantages. First, the VAMNs can be facilely grown using the conventional chemical vapor deposition (CVD) method, permitting easy fabrication and potential mass device production. Second, the unique advantage of the VAMNs for biosensor development lies in its abundant surface-exposed active edge sites that possess a high binding affinity with thiol-based linkers, which overcomes the challenge of molecule functionalization on the conventional planar MoS$_2$ nanolayers. The high binding affinity between 11-mercaptoundecanoic acid and the VAMNs was demonstrated through experimental surface characterization and theoretical calculations via density functional theory. The FET biosensor allows rapid (within 20 min) and ultrasensitive PSA detection in human serum with simple operations (limit of detection: 800 fg mL^{-1}). This FET biosensor offers excellent features such as ultrahigh sensitivity, ease of fabrication, and short assay time, and thereby possesses significant potential for early-stage diagnosis of life-threatening diseases.

* Corresponding author.
  E-mail address: xyliu@mie.utoronto.ca (X. Liu).

1. Introduction

Recently, the graphene-like, two-dimensional molybdenum disulfide (2D MoS$_2$) nanolayers have attracted significant research attention in various fields, including micro/nanoelectronics, optoelectronics, photonics, and chemical catalysis, among others [1–8]. The unique advantage of the MoS$_2$ nanolayer is mainly attributed to its atomically thin structure and layer-dependent material properties such as indirect-to-direct bandgap transition as the layer number decreases, thereby making it a promising semiconducting material for a variety of applications such as photodetectors [9,10], field-effect transistors (FETs) [1,11], and biosensors [12–19]. Several studies have confirmed its remarkable performance in promoting surface-enhanced Raman scattering (SERS) and enhanced photocatalytic (PEC) applications [20–22]. Using planar intrinsic MoS$_2$ for constructing FET devices usually can result in excellent device performances with good on/off ratio, which also benefits the FET biosensor development by leading to low baseline noise and leakage current. However, the FET biosensor is more complicated than the FET device, and the on/off ratio is important [23]. Like other biosensors [24–26], biofunctionalization also plays an essential role in determining the sensitivity, reliability, and fabrication difficulty of FET biosensors. It has been suggested that MoS$_2$ nanolayers possess two distinctive advantages as semiconductor channel materials for FET biosensors [27,28]. First, compared to 2D graphene-based FET biosensors, 2D MoS$_2$-based FET biosensors provide superior analytical performance in terms of sensitivity and limit of detection (LOD) [27]. This advantage can be attributed to the reduced channel current leakage because of a narrow bandgap (1.3–1.9 eV), thereby permitting enhanced performance compared to the zero-bandgap graphene FET biosensors [29–31]. Second, MoS$_2$-based FET biosensors are generally easier to fabricate at a lower cost than one-dimensional (1D) nanomaterials-based (*e.g.*, Si nanowires and carbon nanotubes) FET biosensors [32–35], which have been constructed through wafer-scale manufacturing but still have difficulties including the high-fabrication cost, low fabrication yields and integrability issues [27].

Because of these advantages, 2D MoS$_2$ has been extensively studied for developing FET biosensors after its first introduction into the biosensor community [27]. These devices have been demonstrated for detecting biomolecules such as proteins and nucleic acids [18,30, 36–39]. Despite the rapid progress of MoS$_2$-based FET biosensors, there still exists an inherent challenge for the efficient immobilization of biomolecules (as capture probes) onto the basal plane of 2D MoS$_2$, which hampers the achievement of high sensitivity and reproducibility of the biosensor. Existing methods for capture probe immobilization on MoS$_2$ are primarily based on two methods: (i) chemical modification of an additional dielectric layer (*e.g.*, Al$_2$O$_3$, HfO$_2$) deposited on top of the MoS$_2$-based FET channel [27,30,40], and (ii) physical adsorption of biomolecules on the bare surface of MoS$_2$ nanolayer [36,41,42]. The former method needs to deposit an extra layer of dielectric material on top of the MoS$_2$ nanolayer, which also increases the overall thickness of the channel material by tens of nanometers [30]; this increases the separation between the charged target molecules (bound on the dielectric layer) from the MoS$_2$ channel surface, which will deteriorate the device sensitivity due to the ionic screening effect. The addition of the dielectric layer also increases the complexity of device fabrication [37]. The latter method heavily relies on the Van der Waals force of the MoS$_2$ for biomolecule immobilization. However, the material's large surface with Van der Waals affinity causes the molecules to lie flat on it rather than forming covalent or strong ionic bonds [28,43]. Thus, this approach usually yields relatively low stability and reproducibility of the FET biosensor. In addition, a new approach that utilizes the nickel ions as a short mediating linker on the basal surface of MoS$_2$ nanolayers to bind the nickel-chelating agents has been demonstrated [41]. This method overcomes the aforementioned challenges well and represents a promising route to decorating MoS$_2$ nanolayers with capture probe molecules, though the nickelions can only be limited to several specific probe molecules, such as histidine residues and nickel porphyrins.

The most common chemical routes for direct conjugation of probe molecules on the MoS$_2$ basal plane depend on the active sites (defects, edge sites, and tears) of MoS$_2$ that provide high energy for biomolecule conjugation [44,45]. Among those active sites, the edge sites of MoS$_2$ monolayers are terminated with exposed molybdenum or sulfur atoms containing dangling bonds and having high *d*-orbital electron density, which can act as the robust anchors for thiol-based chemical linkers [45, 46]. However, the surface active sites and edge sites are randomly formed within the MoS$_2$ nanolayer. This randomness leads to high device-to-device and batch-to-batch variations of the MoS$_2$ biofunctionalization and, thus the biosensor performance. Recently, vertically aligned MoS$_2$ nanolayers (VAMNs), consisting of atomically-thin MoS$_2$ crystal structures vertically aligned and packed in a thin-film format, have been successfully synthesized through chemical vapor deposition (CVD)-based Mo sulfurization [47,48]. This method allows for the good controllability of the thickness and orientation of the nanolayers, which are critical for optimizing the biosensor's sensitivity and specificity [47]. In this new form of MoS$_2$ nanostructures, the edge sites of the vertical MoS$_2$ nanolayers are exposed on the top surface of the synthesized MoS$_2$ thin film, providing dense and uniformly distributed active sites for biofunctionalization. This unique surface property of the VAMNs provides one good solution for addressing the technical challenge of MoS$_2$ biofunctionalization and enhancing the interaction between the analyte and biosensor surface. This improves the sensitivity and specificity of biosensors, making the material highly promising as the semiconductor channel of MoS$_2$-based FET biosensors that can detect low concentrations of biomolecules in complex samples. Despite its high surface energy caused by the edge sites, the VAMNs have been proven stable under ambient conditions [47]. A previous study has also demonstrated the enhanced gas molecules absorption on the edge sites of the VAMNs [49], showing the great potential of the VAMNs for biosensor development. The development of ultrasensitive biosensors, including this technology, has good implications for various applications such as disease diagnosis, antibiotic determination, and environmental monitoring [19,23,50–52].

In this article, we report the first FET biosensor that integrates micropatterned VAMNs as the biosensing FET channel for label-free and ultrasensitive prostate-specific antigen (PSA) detection. The VAMNs-based FET channels are batch-synthesized through CVD-based rapid sulfurization of pre-patterned Mo thin films. We demonstrate the high binding affinity of surface edge sites of the VAMNs with thiol-based chemical linkers (11-MUA), which is validated by various techniques, including X-ray photoelectron spectroscopy (XPS), atomic force microscopy (AFM), and density-functional theory (DFT) calculations. We also calibrated the FET biosensor using human serum spiked with purified PSA, and achieved an LOD of 800 fg mL^{-1} (>10 times lower than that of a commercial ELISA kit for PSA testing). This VAMNs-based FET biosensor represents a new advancement in the MoS$_2$-based biosensors and holds great potential for early-stage disease diagnosis.

2. Results and discussion

2.1. Design of the VAMNs-based FET biosensor

Fig. 1a shows the schematic design of the VAMNs-based FET biosensor with an enlarged view of the VAMNs channel area, which consists of one VAMNs-based FET and one polydimethylsiloxane (PDMS) reservoir for confining the sample solution in the FET channel area during a test. The FET was batch-fabricated on a three-inch silicon substrate with an intermediate layer of SiO$_2$ (280 nm) for insulating the biosensors from the silicon substrate. As shown in Fig. S1, a 1 mm × 1 mm pattern of Mo thin film (15 nm) was first deposited onto the SiO$_2$-coated wafer through Mo sputtering and then lift-off patterning. Then, the Mo pattern was converted into VAMNs through CVD-based rapid sulfurization (see details in the latter part of this section). The 1 mm × 1

mm size of the VAMNs facilitates the alignment of the source and drain electrodes to be deposited on top of the VAMNs. The length (*L*) and width (*W*) of the FET channel are defined by the gap size between the source and drain electrodes, which are 30 μm and 900 μm, respectively (*W/L* ratio: 30). The source/drain electrodes were made of a titanium/gold bilayer (15/30 nm) that have been commonly used in MoS$_2$-based FETs for forming Ohmic contacts [1,30]. A key design consideration of FET biosensors is the electrical insulation of the two electrodes from the sample solution. Without proper insulation, the direct binding of target molecules on the electrode surfaces may occur and therefore alter the work function of the electrode/VAMNs pair [53]; poor electrode insulation will also cause leaking currents from the electrode to the sample solution [53].

To eliminate this issue, we insulated the electrodes by atomic layer deposition (ALD) of a 30 nm Al$_2$O$_3$ layer, but left the FET channel area and the two contact pad areas open to the target solution and external probes, respectively. In some studies [27,54,55], Al$_2$O$_3$, a high-k material, has been proven suitable for passivation and has performed well in practical applications of biosensors. In the future, we could adopt a better passivation layer like HfO$_2$ (a high-k dielectric) that can solve ion transport instability and other problems of biosensor use by passivating the exposed surface [56–60]. The circular reservoir containing the sample solution was made from PDMS, which was widely used to fabricate microfluidic channels in biosensors thanks to its chemical inertness [30]. The reservoir was designed to be 2 mm in diameter and 15 mm in height, and was fabricated to punch a 2 mm-diameter through-hole on a 15 mm PDMS cube. The reservoir was placed on the FET biosensor, and the alignment of the reservoir and the FET channel area was conducted under a stereo microscope. The seal of the PDMS reservoir was ensured by the physical adhesion of the PDMS on the device surface. The reservoir can hold up to 50 μL solution. The microscopic photograph of the FET channel area of a fabricated device is shown in Fig. 1b.

For testing the FET, a miniaturized Ag/AgCl reference electrode of 2 mm diameter (ET072-1, eDAQ Inc.) was inserted into the circular reservoir as the gate electrode for regulating the gate voltage (Fig. 1c), and it also served as a seal of the reservoir to prevent solution evaporation. Compared to other commonly-used in-liquid gate electrodes, such as Pt wires, the Ag/AgCl gate electrode can provide stable regulating voltages and is non-polarizable [61]. To perform an assay for PSA detection, we added 30 μL of PSA sample into the PDMS reservoir for direct contact with the biofunctionalized VAMNs channel. The reservoir was then closed by inserting the Ag/AgCl gate electrode, and the contact between the sample solution and the gate electrode was confirmed through visual inspection. The biosensor was then incubated for 30 min at room temperature to allow thorough conjugation of the PSA with its capture probe on the VAMNs [30]. Finally, the FET current-voltage (I–V) characteristic was measured by a precision source meter.

2.2. Growth and characterization of the VAMNs

For MoS$_2$ synthesis, mechanical exfoliation has been widely used to produce high-quality MoS$_2$ mono- or few-layers for transfer onto another substrate for FET fabrication. However, this method is less feasible for device mass production because of its low yield and incapability of patterning an array of MoS$_2$ nanolayers on a substrate [28]. In contrast, CVD-based approaches are more promising for large-scale growth and patterning of MoS$_2$ [62,63]; in particular, CVD-based sulfurization of a Mo seed thin film (using sulfur vapor) has been used to grow stable VAMNs on a large scale [47]. The mechanism of the sulfurization method is based on the diffusion of sulfur vapor into the Mo seed film, which converts Mo into sulfide. The mass transport of the sulfur vapor through van der Waals gaps between the vertically formed MoS$_2$ nanolayers is much faster than that laterally across the MoS$_2$ nanolayers [47]. As a result, the formed MoS$_2$ nanolayers tend to be perpendicular to the substrate (Fig. 2a), exposing the van der Waals gaps maximally and providing rich edge sites for thiol-based linkers for faster reaction. These linkers have a higher binding affinity to immobilize probes than conventional sensing materials. The VAMNs growth and subsequent FET fabrication processes are compatible with standard microfabrication techniques, which are briefly described here (see details in the Supplementary Information). We first deposited a 15 nm Mo layer onto a SiO$_2$-coated silicon wafer, during which a lift-off process was used to pattern the Mo layer into 1 mm × 1 mm squares (for forming VAMN thin-film patterns). We then placed the wafer into a CVD furnace tube and loaded elemental sulfur powder at the upstream of the wafer. By setting a temperature gradient in the tube, we conducted the sulfurization process under a continuous flow of argon gas for 30 min to convert the Mo layer into VAMNs.

To examine the synthesized VAMNs, we first confirmed the chemical bond states of the VMANs using XPS. There are two peaks at 229.1 eV and 232.3 eV observed in the Mo 3s spectrum (Fig. 2b), which can be attributed to the doublet of Mo 3d$_{5/2}$ and Mo 3d$_{3/2}$, respectively. The S 2p spectrum is shown in Fig. 2c, and the two peaks at binding energy levels of 161.9 eV and 163.1 eV can be assigned to the spin-orbit S 2p$_{3/2}$ and S 2p$_{1/2}$, respectively. The observed XPS spectra of the VAMNs are in good agreement with previously reported data [63], demonstrating the successful growth of the VAMNs. Transmission electron microscopy (TEM) imaging was then utilized to visualize the VAMNs directly. Further structural characterization of the VAMNs provides additional
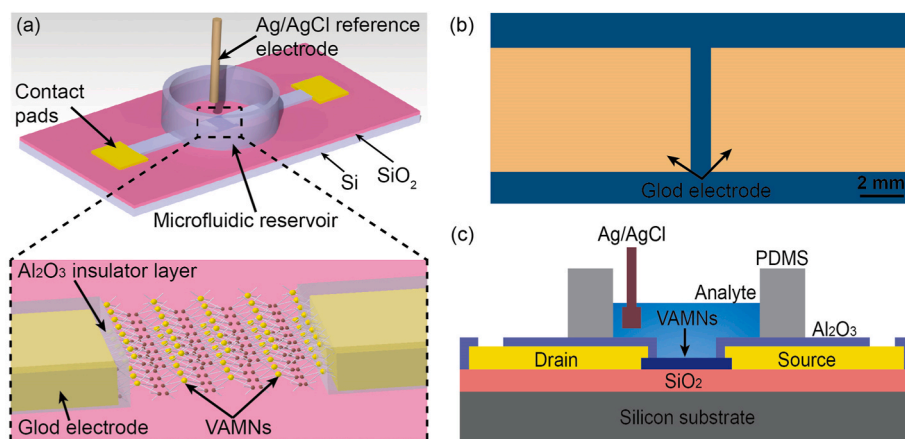

Fig. 1. Device design and testing setup. (a) Schematic diagram of the VAMNs-based FET biosensor design with an enlarged view of the VAMNs channel area. (b) Photograph of the synthesized VAMNs with two gold electrodes patterned on top. The length and width of the FET channel area are 30 μm and 900 μm, respectively. (c) Schematic diagram of the device testing setup.
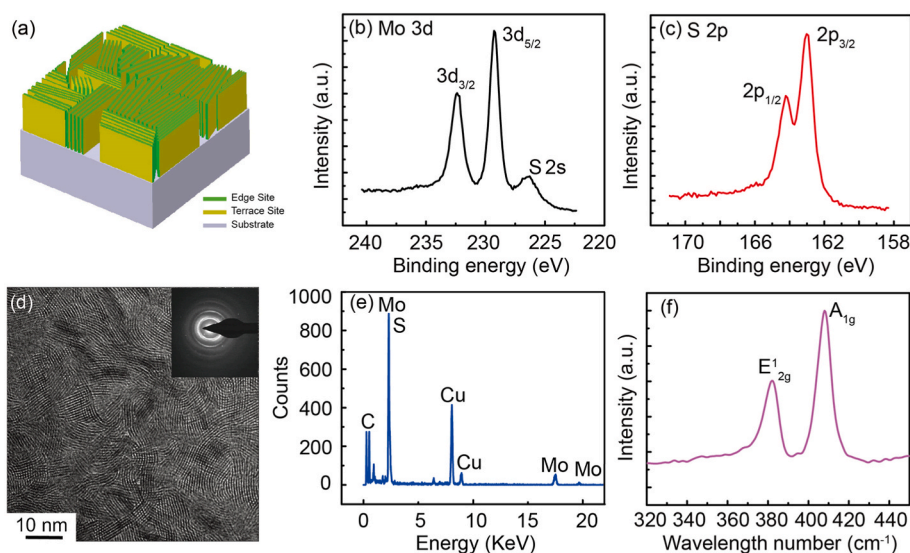
Fig. 2. Growth and characterization of the VAMNs. (a) Schematic of the VAMNs with the layers aligned perpendicular to the substrate, maximally exposing the edges of the layers. (b)(c) XPS spectra of a VAMN film for: (b) Mo 3 d, where the two peaks at 229.1 eV and 232.3 eV are attributed to the doublet Mo $3d_{5/2}$ and Mo $3d_{3/2}$, respectively; (c) S 2p, where the two peaks at 161.9 eV and 163.1 eV are attributed to the spin-orbit S $2p_{3/2}$ and S $2p_{1/2}$, respectively. (d) TEM images of the VAMNs. (e) EDX spectrum of VAMNs. (f) Raman spectrum of the VAMNs showing a higher intensity peak at A_{1g} than E_{2g}^1, reflecting the dominantly exposed MoS$_2$ edge sites [47,49].

insights. Fig. 2d directly visualizes VAMNs using transmission electron microscopy (TEM) imaging. This TEM image of a typical MoS$_2$ film shows the individual atomic planes arranged in a specific order forming each layer. Furthermore, Fig. 2d clearly reveals the large area of stripe-like nano-grain structures, indicating the densely packed edges of the synthesized VAMNs exposed on the material surface [47]. The selective area electron diffraction (SEAD) patterns show the polycrystalline diffraction spots suggesting the synthesized thin-film VAMNs are polycrystalline, which is also consistent with the previous study [47].

The energy dispersiveX-Ray (EDX) spectrum of TEM (Fig. 2e) also clearly shows Mo, S, Cu, and carbon peaks, suggesting the correct chemical compositions. Note that the Cu and carbon peaks came from the supporting TEM grid. We also performed Raman spectroscopy to investigate the orientation (planar or vertically aligned) of the VAMNs. The Raman spectrum shows peaks at 383 cm^{-1} and 408 cm^{-1} (Fig. 2f), which correspond to the in-plane (E_{2g}^1) and out-of-plane (A_{1g}) vibration modes of the MoS$_2$ bonding, respectively [47]. It can be observed that the out-of-plane vibration mode of the Mo–S bond is predominately excited due to the dominantly exposed edge sites, yielding a higher intensity of the A_{1g} peak over the E_{2g}^1 peak (Fig. 2f). This result agrees well with previously reported Raman spectra of the VAMNs [47], and provides clear evidence of the successful growth of the VAMNs. The stability of biomolecule immobilization is crucial for the stability and reproducibility of FET biosensors [64]. MoS$_2$ immobilizes biomolecules via 2D molecular layers connected by van der Waals forces in the crystal structure [47], rather than forming covalent or strong ionic bonds [28, 43]. In contrast to methods that heavily rely on van der Waals forces, our VAMNs were successfully grown and validated through above experiments, presenting a nearly ideal edge-terminated structure (large striped nanograin structure) that is stable in the environment.

2.3. Biofunctionalization of the VAMNs channel

Thiol chemistry is one of the most prevailing chemical routes to chemical modification of the MoS$_2$ surface because the active sites (defects, edge sites, and tears) of the MoS$_2$ basal plane possess high thiol-molecular affinities and thus can facilitate the absorption of thiol ligands. The edge sites mainly serve as chemical conjugation anchors, as demonstrated in previous studies [44,45]. Therefore, we used thiol chemistry to conjugate a commonly-used thiol-based linker, 11-mercaptoundecanoic acid (11-MUA), and the abundant surface exposed edge sites of the VAMNs significantly improved the quantity and the uniformity of the 11-MUA linkers conjugated on the top surface of VAMN,

which enabled the excellent analytical performance of the VAMNs-based FET biosensor. Then the aqueous solutions of N-(3-Dimethylaminopropyl)-N′-ethyl carbodiimide hydrochloride (EDC) and N-Hydroxysuccinimide (NHS) were used to activate the carboxyl groups of the sensing probe. Finally, the probe protein molecule was added to biofunctionalize the VAMNs surface (Fig. 3).

We first optimized the experimental condition of 11-MUA conjugation with VAMNs. Two major experimental parameters are the concentration of 11-MUA in ethanolic solution and the incubation time. The previously adopted concentrations of 11-MUA are usually in the range of 0.1 mM to 0.1 M, which has been confirmed to have no observable influence on the conjugation result [45,65]. Thus, we set the 11-MUA concentration to 0.1 M. We then optimized the incubation time by characterizing the conjugation uniformity using AFM imaging. Using AFM to characterize a self-assembled monolayer (SAM, ~2 nm) of 11-MUA is technically challenging. However, according to the previous study, the multilayer of 11-MUA (6–12 nm) will be formed above the 11-MUA SAM and can be used as an AFM-readable sign for 11-MUA SAM formation (the multilayer 11-MUA will be desorbed under ambient environment and leave 11-MUA SAM on the substrate) [65]. Therefore, the AFM is suitable for our purpose of surface characterization.

Fig. 4a–c shows the AFM images of the VAMNs before 11-MUA conjugation and after 12-h and 24-h incubation in the 11-MUA solution, respectively. For comparison, planar MoS$_2$ nanolayers were also conjugated with 11-MUA, and AFM images of the planar MoS$_2$ surfaces with the same conjugation conditions (*i.e.*, before conjugation and after 12-h and 24-h conjugation) are shown in Fig. 4d–f, respectively. To well compare the images under different conditions, the scale bar was adjusted to the same range and color rendering. As shown in Fig. 4a and d, both the VAMNs and planar MoS$_2$ have uniform surface morphologies before conjugation. After 12-h incubation in the 11-MUA solution, islands of 11-MUA multiplayer with a height of ~6 nm were formed on the VAMNs surface (Fig. 4e). However, only ~30% of the scanning area (10 μm × 10 μm) was covered by the 11-MUA multilayers. After increasing the incubation time to 24 h, the coverage of 11-MUA on the VAMNs was significantly improved to ~90% (Fig. 4f). Therefore, 24-h incubation was used for chemical modification of the VAMN channel of the FET biosensor. In contrast, the planar MoS$_2$ only has small islands of 11-MUA after 24-h incubation, indicating that the lack of densely packed active sites on the planar MoS$_2$ surface limits the chemical conjugation of the 11-MUA. The degree of molecular functionalization depends strongly on the immobilization efficiency of the probes [66]. After the same incubation time (12 h and 24 h), as determined by the scale of 11-MUA islands shown in AFM images, VAMNs with high
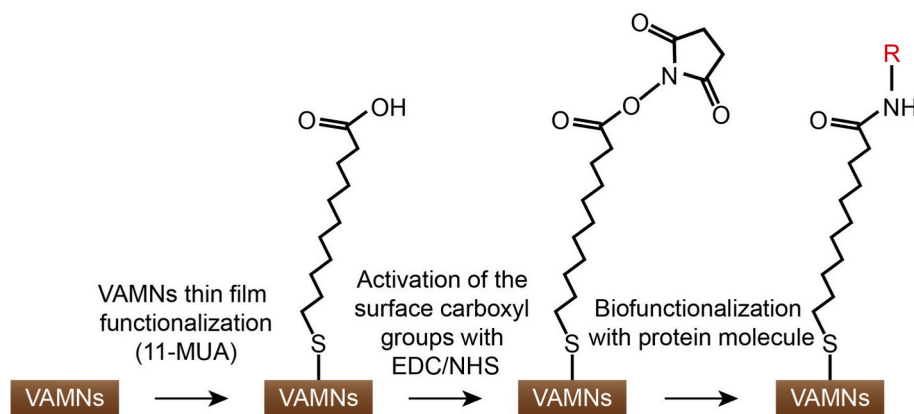
Fig. 3. Schematic diagram of the surface chemistry for biofunctionalization of the top surface of the VAMNs thin film. The probe protein molecule in the final step is denoted as 'R'.
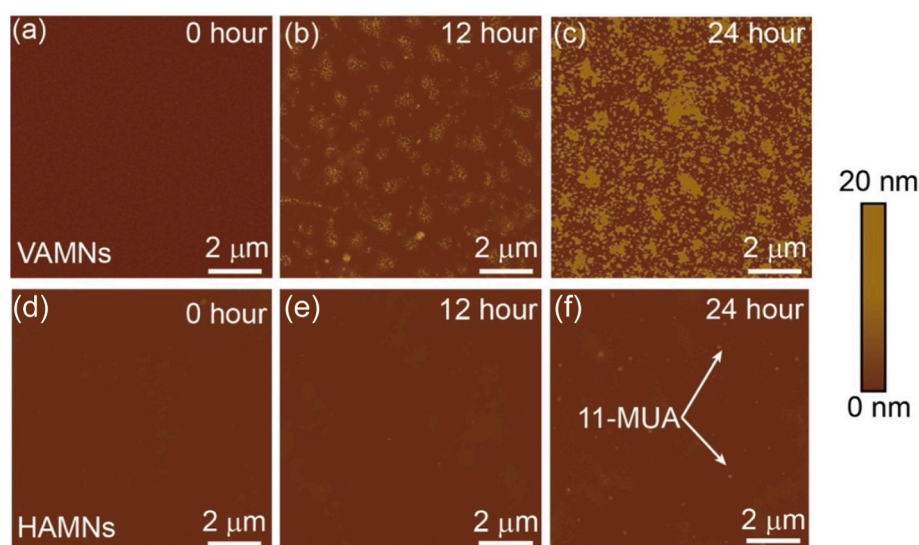

Fig. 4. AFM characterization of 11-MUA conjugation on VAMNs and planar MoS$_2$. (a–c) AFM images of the VAMNs before conjugation and after 12-h and 24-h conjugation, respectively. (d–f) AFM images of planar MoS$_2$ surfaces with the same conjugation conditions, *i.e.*, before conjugation and after 12-h and 24-h conjugation, respectively.

binding affinity to thiol-based linkers have higher immobilization efficiency than planar MoS$_2$. Lastly, the PSA antibodies were conjugated with the 11-MUA to serve as the anti-PSA capture probe on the FET channel, through a 60-min incubation in 10 μg mL^{-1} anti-PSA solution.

To verify the surface conjugation of 11-MUA and VAMNs, XPS analysis was performed. The C 1s and S 2p core level spectra for pristine and 11-MUA-conjugated VAMNs were fitted according to methods used in previous studies [45]. As shown in Fig. 5a, the pristine VAMNs contained only one C 1s peak at 284.8 eV (arising from the environment containment). Only two representative S 2p doublet peaks of VAMNs were observed at binding energy levels of 161.7 eV and 163.2 eV (Fig. 5b). In the 11-MUA-conjugated VAMNs, there are two additional peaks revealed at 289.4 eV (-COOH) and 287.4 eV (C–S) (Fig. 5c). As shown in Fig. 5d, the second component in the S 2p core level at higher binding energies (165.7 eV and 164.5 eV) was observed unequivocally, which corresponds to the C–S binding peaks resulting from the conjugation of 11-MUA and VAMNs. The XPS spectra confirm the successful 11-MUA conjugation on the VAMNs, and were in good agreement with the previously reported ex-MoS$_2$ conjugation with MUA [45].

To investigate the 11-MUA adsorption behaviors on MoS$_2$ nanolayers with different alignments, DFT calculations were conducted to compute the adsorption energy of 11-MUA under each alignment configuration.

Because the Mo edge atoms prefer to be coordinately saturated by adsorption of additional S atoms under certain conditions [67,68], the DFT calculations were extended to two different coverages of S (50% and 100%) on the Mo edge, along with the basal plane, Mo edge, and S edge. The configurations for Mo edge terminations with 50% and 100% S-coverages followed the ones presented by Seivane et al. [69]. The aforementioned five systems were expanded into supercells to reduce the interactions between the periodic images of the 11-MUA molecules, as illustrated in Fig. 6.

The slab model was used with different MoS$_2$ layers (one horizontally aligned layer in the basal plane and three vertically aligned layers in edge terminations) in all the calculations, which were sufficiently large to obtain convergence of the 11-MUA adsorption energy values. The snapshots of optimized 11-MUA adsorption configurations near different MoS$_2$ terminations are shown in Fig. 6. In the configurations of the basal plane (Fig. 6a), S edge (Fig. 6b), Mo edge (Fig. 6c), 50% S-coverage Mo edge (Fig. 6d), and 100% S-coverage Mo edge (Fig. 6e), the computed adsorption energy values are 0.80 eV, −2.15 eV, 0.69 eV, −0.64 eV and −2.36 eV, respectively. The C–S bond length (1.84 Å) of 11-MUA adsorbed on the edge terminations is shorter than that (1.88 Å) of the basal plane, indicating that the 11-MUA molecule binds more strongly to the edge terminations compared to the basal plane
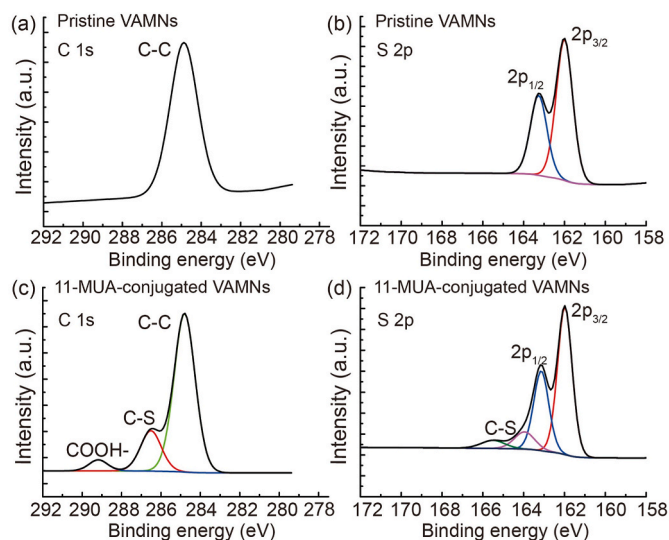
Fig. 5. XPS spectra before and after 11-MUA conjugation. (a)(c) C 1s XPS spectra of (a) pristine VAMNs and (c) 11-MUA conjugated VAMNs. (b)(d) S 2p XPS spectra of (b) pristine VAMNs and (d) 11-MUA conjugated VAMNs.

configuration. This is consistent with our experimental data showing superior molecule adsorption properties of the VAMN edge sites. It is difficult to experimentally identify the precise atomic compositions along with the edge layers; thus, the DFT calculations for different configurations of the edge layers all lead to stronger 11-MUA binding, which is sufficient to confirm the agreement between the computational and experimental results.

2.4. PSA detection with the VAMNs-based FET biosensor

The sensing performance of FET devices depends on their output and transfer characteristics, which are fundamental factors of an FET. We characterized the electrical properties of the VAMNs-based FET at each step of channel biofunctionalization (11-MUA conjugation and anti-PSA binding). We adopted a similar method by Chen et al. [19] with characteristic curves to prove that anti-PSA was successfully attached to the FET biosensor. As shown in Fig. 7a, the conductance of the FET channel decreased from its intrinsic value of 0.713 mS to 0.637 mS (−10.6%) after 11-MUA conjugation, and then from 0.637 mS to 0.451 mS (−29.2%), after and anti-PSA binding. Here, adding 11-MUA decreases

the conductance of the FET channel because 11-MUA attaches to the FET surface, changing its carrier density and thus increasing its resistance. Furthermore, after anti-PSA was attached to the FET biosensor successfully, it was found that the slope of the output and transfer curves within the working region decreased, which is consistent with previous studies [19,55]. That is because the attachment of a positively charged molecule (anti-PAS) to the FET biosensor corresponds to a positive potential gating, leading to a decrease in the charge carrier density and, thus, a decrease in the conductivity of the FET channel [70,71].

We then performed solution-gate transistor measurement in 0.005× phosphate-buffered saline (PBS) to characterize the transport properties of the device after each step of channel biofunctionalization. It can be observed from Fig. 7b that when V_{gs} changed from −0.4 V to 0.4 V and the V_{ds} remained at 0.1 V (detailed measurement setup is described in the Supplementary Information), I_{ds} changed from 106 nA to 96 nA, showing a *p*-type device characteristic. We also monitored the gate current leakage (labeled in Fig. 7c) occurring simultaneously during gate voltage sweeping. It shows that the gate current leakage is below 250 pA (Fig. 7d), which is hundreds of times lower than the signal current (in the range of tens of nanoamps). The observed *p*-type VAMNs are also consistent with the previous study of VAMNs [35]. After the 11-MUA and anti-PSA conjugation, the device shows obvious carrier mobility degradation as the slopes of the FET transport curves become much smaller and the on/off ratio of the devices decreased from 1.10 to 1.02. The biosensing mechanism in the FET (or FET-like) devices could be complicated that cannot be explained solely by the field-effect principles, where good on/off ratio is favorable [70,72]. In our VAMN biosensors, the carrier mobility degradation (on/off ratio decrease) and the decrease of the FET-channel conductance can be explained by two possible mechanisms [71]. First, due to the lack of a thick dielectric layer on the top of the VAMNs, the charged 11-MUA and PSA antibody may directly induce the disordered potential in the VAMNs and thereby degrade the channel mobility and conductance, like the mechanism reported in vertically-aligned graphene biosensors [37,70,71]. Second, the conjugation of 11-MUA and PSA antibodies may cause local geometric deformation and increase the number of scattering centers across the VAMNs, thereby decreasing the FET channel conductance [71].

We then calibrated the analytical performance of the VAMNs-based FET biosensor using human serum spiked with PSA antigen at different concentrations. Prostate cancer (PCa) has been reported to account for ~10% of all deaths from cancer [73], and PSA is one of the most common serum biomarkers currently available for PCa diagnosis. The ultrasensitive detection of a small trace of PSA in human serum allows physicians to detect prostate tumors at an early stage, thereby
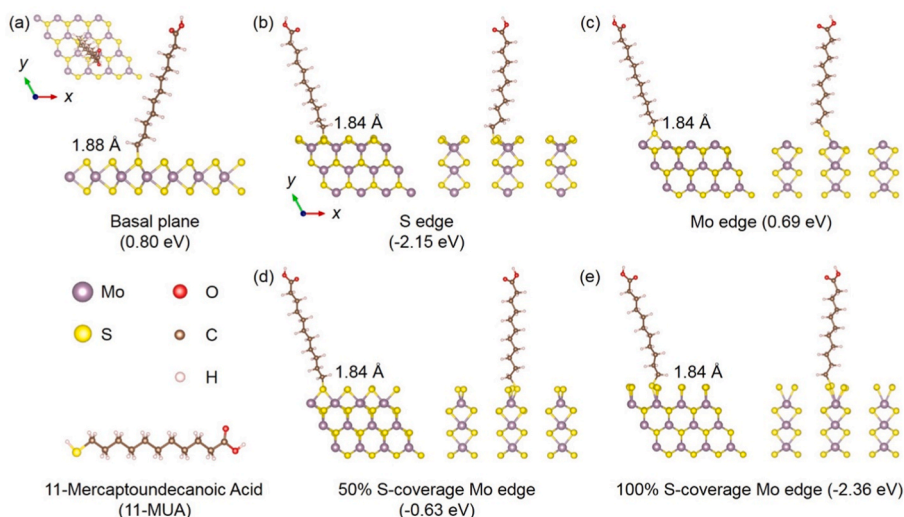

Fig. 6. Snapshots of conjugated 11-MUA configurations on the (a) basal plane, (b) S edge, (c) Mo edge, (d) 50% S-coverage Mo edge, and (e) 100% S-coverage Mo edge. The vacuum region extends along the z-direction for the basal plane case and along the y-direction for the edge cases. In the rest of the directions, the MoS$_2$ atoms are fully periodic with two layers of Mo atoms separated by 6.32 Å (determined from DFT relaxation) along the z-direction (three layers of MoS$_2$ are shown in the illustrations for visualization purposes). The bond length of C–S and the binding energy values of 11-MUA molecules are shown in this Figure. Purple, yellow, red, brown, and white spheres represent molybdenum, sulfur, oxygen, carbon, and hydrogen, respectively. (For interpretation of the references to color in this figure legend, the reader is referred to the Web version of this article.)
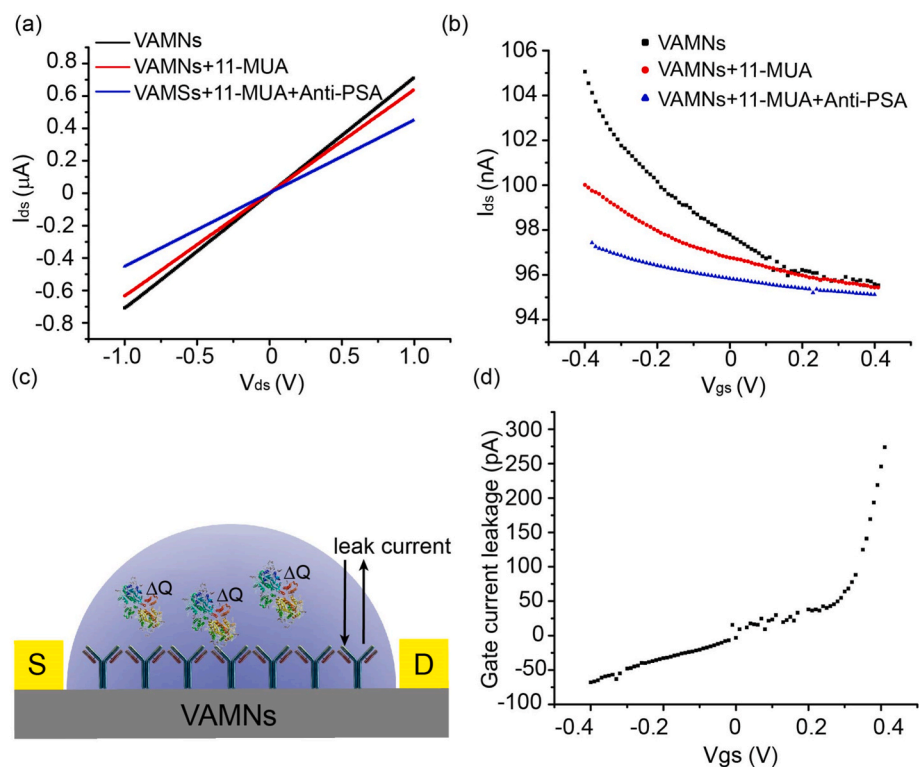
Fig. 7. Electrical characterization of the VAMNs-based FET biosensor. (a) Direct current measurement results of the device modified with 11-MUA (0.1 M) and anti-PSA antibody (10 μg mL^{-1}). (b) Transistor measurement results of the FET biosensor modified with 11-MUA (0.1 M) and anti-PSA antibody (10 μg mL^{-1}). (c) Schematic diagram of the binding event during sensing measurement. (d) Gate current leakage measurement during the transistor measurement indicates the leakage current is < 100 times lower than the signal current.

enabling more timely treatment and decreasing the PCa death rate. As mentioned, 10 μg mL^{-1} PSA antibody solution was used to immobilize the probe molecules on the VAMNs FET channel. The commercial human serum (PSA-free), spiked with purified PSA antigen at different concentrations, was tested using the FET biosensor. Considering the high ionic strength of the human serum with a Debye length of around ~0.7 nm, the serum sample must be diluted with low ionic strength solutions to reduce the ionic screening effect [74,75]. 0.005× PBS at pH of 6 was used to dilute the serum sample 100 times, as its Debye length (~10.7 nm) is sufficiently long to cover the full length of the 11-MUA linker and the PSA antibody-antigen pair [76]. A PSA assay, including sample addition, incubation, and signal readout, typically takes less than 20 min with a fully prepared FET biosensor.

Representative drain-gate I–V curves obtained from the PSA calibration experiments are shown in Fig. 8a. It can be observed that the source-to-drain current decreases with the increase of the PSA concentration, which is also consistent with our theoretical prediction. As discussed, the binding of PSA antigen to the FET channel could lead to

local geometric deformation and increase the number of scattering centers; this effect reduces the channel conductivity, as reported in a previous study [70]. Another mechanism of the FET-based biosensing could be based on the *p*-type characteristic of the VAMNs-based FET. With a mildly acidic isoelectric point (pI) of ~6.9, the PSA antigen will be positively charged at pH = 6. Therefore, the attachment of the positively charged PSA antigen to the VAMNs channel causes a positive potential gating effect that reduces the hole density, therefore, the electrical conductivity of the VAMNs. The calibration data of the FET biosensor are shown in Fig. 8b, which were fitted in an S curve based on the Hill equation. The LOD was determined to be 800 fg mL^{-1}, at least 10 times lower than that of a commercial ELISA kit for PSA testing (ab264615 Human PSA ELISA Kit, Abcam, whose sensitivity data is 8 pg mL^{-1}) [77]. This analytical performance of our VAMNs-based FET biosensor shows significant potential for early-stage clinical testing of PCa.
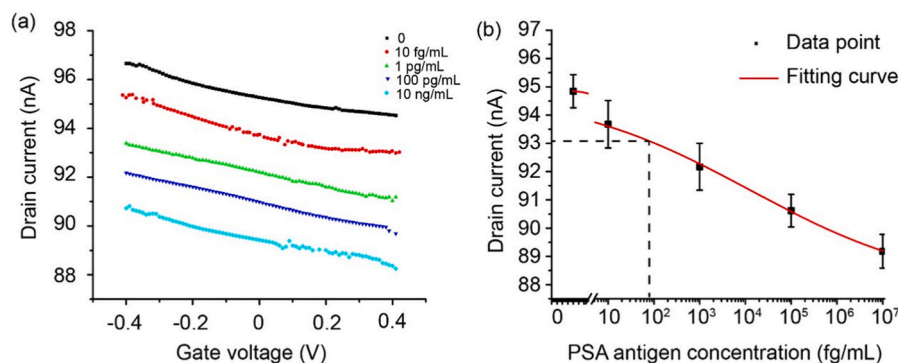

Fig. 8. Detection of PSA antigen in human serum. (a) Representative transport curves in response to human serum samples spiked with PSA antigen at increased concentrations. (b) Calibration data of the VAMNs-based FET biosensor for quantification of PSA antigen spiked in human serum samples, with data fitted into an S curve (N = 8).

3. Conclusion

We reported the first FET biosensor integrating semiconductive VAMNs as the FET channel for label-free and ultrasensitive immunoassays. The rapid sulfurization process for VAMNs growth allows the facile patterning of the FET channels, which is compatible with conventional microfabrication processes and enables wafer-scale batch fabrication of the FET biosensor. Through experimental characterization and theoretical calculations, the abundant edge sites of the thin-film surface of VAMNs have been proven to be active sites for thiol-based linker conjugation and capture probe functionalization. Using PCa as a real disease model, we calibrated the FET biosensors using PSA-spiked serum samples and achieved an ultralow LOD of 800 fg mL^{-1} (>10 times lower than that of a commercial ELISA kit). The VAMNs-based FET biosensor represents a new advance in the field of MoS$_2$-based biosensors and holds great potential in early-stage disease diagnostics.

CRediT authorship contribution statement

Pengfei Song: Conceptualization, Investigation, Visualization, Writing - original draft, Writing - review & editing. **Pengfei Ou:** Visualization, Methodology. **Yongjie Wang:** Investigation. **Hang Yuan:** Writing – review & editing. **Sixuan Duan:** Writing – review & editing. **Longyan Chen:** Conceptualization. **Hao Fu:** Methodology. **Jun Song:** Methodology. **Xinyu Liu:** Supervision, Conceptualization, Funding acquisition, Writing - review & editing.

Declaration of competing interest

The authors declare that they have no known competing financial interests or personal relationships that could have appeared to influence the work reported in this paper.

Data availability

Data will be made available on request.

Appendix A. Supplementary data

Further details on VAMNs sensor fabrication, CVD growth of vertically aligned MoS$_2$ nanolayers and snapshots of most stable configurations for the basal plane, S edge, Mo edge, 50% S-coverage Mo edge, and 100% S-coverage Mo edge with a single sulfur vacancy on the surface. And the details of experimental methods are also provided.

Supplementary data to this article can be found online at https://doi.org/10.1016/j.aca.2023.341036.

References

[1] B. Radisavljevic, A. Radenovic, J. Brivio, V. Giacometti, A. Kis, Single-layer MoS$_2$ transistors, Nat. Nanotechnol. 6 (2011) 147–150.

[2] D. Kufer, G. Konstantatos, Highly sensitive, encapsulated MoS$_2$ photodetector with gate controllable gain and speed, Nano Lett. 15 (2015) 7307–7313.

[3] G. Li, D. Zhang, Q. Qiao, Y. Yu, D. Peterson, A. Zafar, R. Kumar, S. Curtarolo, F. Hunte, S. Shannon, All the catalytic active sites of MoS$_2$ for hydrogen evolution, J. Am. Chem. Soc. 138 (2016) 16632–16638.

[4] O. Salehzadeh, M. Djavid, N.H. Tran, I. Shih, Z. Mi, Optically pumped two-dimensional MoS$_2$ Lasers operating at room-temperature, Nano Lett. 15 (2015) 5302–5306.

[5] M. Zhu, X. Du, S. Liu, J. Li, Z. Wang, T. Ono, A review of strain sensors based on two-dimensional molybdenum disulfide, J. Mater. Chem. C 9 (2021) 9083–9101.

[6] H.K. Adigilli, A. Pandey, J. Joardar, 2D-nanolayered Tungsten and Molybdenum Disulfides: Structure, Properties, Synthesis, and Processing for Strategic Applications. *Handbook of Advanced Ceramics and Composites: Defense, Security, Aerospace and Energy Applications*, 2020, pp. 75–120.

[7] J.S. Ponraj, M.V. Narayanan, R.K. Dharman, V. Santiyagu, R. Gopal, J. Gaspar, Recent advances and need of green synthesis in two-dimensional materials for energy conversion and storage applications, Curr. Nanosci. 17 (2021) 554–571.

[8] D. Gupta, V. Chauhan, R. Kumar, A comprehensive review on synthesis and applications of molybdenum disulfide (MoS$_2$) material: past and recent developments, Inorg. Chem. Commun. 121 (2020), 108200.

[9] O. Lopez-Sanchez, D. Lembke, M. Kayci, A. Radenovic, A. Kis, Ultrasensitive photodetectors based on monolayer MoS$_2$, Nat. Nanotechnol. 8 (2013) 497–501.

[10] X. Liu, S. Hu, J. Luo, X. Li, J. Wu, D. Chi, K.W. Ang, W. Yu, Y. Cai, Suspended MoS$_2$ photodetector using patterned sapphire substrate, Small 17 (2021), 2101298.

[11] F. Wu, H. Tian, Y. Shen, Z. Hou, J. Ren, G. Gou, Y. Sun, Y. Yang, T.-L. Ren, Vertical MoS$_2$ transistors with sub-1-nm gate lengths, Nature 603 (2022) 259–264.

[12] Y. Huang, J. Guo, Y. Kang, Y. Ai, C.M. Li, Two dimensional atomically thin MoS$_2$ nanosheets and their sensing applications, Nanoscale 7 (2015) 19358–19376.

[13] D. Lembke, A. Kis, Breakdown of high-performance monolayer MoS$_2$ transistors, ACS Nano 6 (2012) 10070–10075.

[14] X. Wang, P. Wang, J. Wang, W. Hu, X. Zhou, N. Guo, H. Huang, S. Sun, H. Shen, T. Lin, Ultrasensitive and broadband MoS$_2$ photodetector driven by ferroelectrics, Adv. Mater. 27 (2015) 6575–6581.

[15] T. Deng, S. Li, Y. Li, Y. Zhang, J. Sun, W. Yin, W. Wu, M. Zhu, Y. Wang, Z. Liu, Polarization-sensitive photodetectors based on three-dimensional molybdenum disulfide (MoS$_2$) field-effect transistors, Nanophotonics 9 (2020) 4719–4728.

[16] P. Masih Das, M. Drndić, In *situ* 2D MoS$_2$ field-effect transistors with an electron beam gate, ACS Nano 14 (2020) 7389–7397.

[17] S. Barua, H.S. Dutta, S. Gogoi, R. Devi, R. Khan, Nanostructured MoS$_2$-based advanced biosensors: a review, ACS Appl. Nano Mater. 1 (2018) 2–25.

[18] X. Gan, H. Zhao, X. Quan, Two-dimensional MoS$_2$: a promising building block for biosensors, Biosens. Bioelectron. 89 (2017) 56–71.

[19] X. Chen, S. Hao, B. Zong, C. Liu, S. Mao, Ultraselective antibiotic sensing with complementary strand DNA assisted aptamer/MoS$_2$ field-effect transistors, Biosens. Bioelectron. 145 (2019), 111711.

[20] M.S.S. Bharati, V.R. Soma, Flexible SERS substrates for hazardous materials detection: recent advances, Opto-Electron. Adv. 4 (2021) 210048, 210041.

[21] C. Zhang, C. Ji, J. Yu, Z. Li, Z. Li, C. Li, S. Xu, W. Li, B. Man, X. Zhao, MoS$_2$-based multiple surface plasmonic coupling for enhanced surface-enhanced Raman scattering and photoelectrocatalytic performance utilizing the size effect, Opt Express 29 (2021) 38768–38780.

[22] C. Zhang, Z. Li, S. Qiu, W. Lu, M. Shao, C. Ji, G. Wang, X. Zhao, J. Yu, Z. Li, Highly ordered arrays of hat-shaped hierarchical nanostructures with different curvatures for sensitive SERS and plasmon-driven catalysis, Nanophotonics 11 (2022) 33–44.

[23] P. Song, H. Fu, Y. Wang, C. Chen, P. Ou, R.T. Rashid, X. Liu, A microfluidic field-effect transistor biosensor with rolled-up indium nitride microtubes, Biosens. Bioelectron. 190 (2021), 113264.

[24] W. Yuan, H. Yuan, K. Jiao, J. Zhu, E.G. Lim, I. Mitrovic, P. Song, Facile microembossing process for microchannel fabrication for nanocellulose-paper-based microfluidics, ACS Appl. Mater. Interfaces 15 (2023) 6420–6430.

[25] B. Fong, Self-Cognizant bionic liquid sensor for pathogen diagnosis, Cyborg Bionic Syst. 2021 (2021), 9861513.

[26] H. Wang, J. Kan, X. Zhang, C. Gu, Z. Yang, Pt/CNT micro-nanorobots driven by glucose catalytic decomposition, Cyborg Bionic Syst. 2021 (2021), 9876064.

[27] D. Sarkar, W. Liu, X. Xie, A.C. Anselmo, S. Mitragotri, K. Banerjee, MoS$_2$ field-effect transistor for next-generation label-free biosensors, ACS Nano 8 (2014) 3992–4003.

[28] K. Kalantar-zadeh, J.Z. Ou, Biosensors based on two-dimensional MoS$_2$, ACS Sens. 1 (2016) 5–16.

[29] D.-W. Lee, J. Lee, I.Y. Sohn, B.-Y. Kim, Y.M. Son, H. Bark, J. Jung, M. Choi, T.H. Kim, C. Lee, Field-effect transistor with a chemically synthesized MoS$_2$ sensing channel for label-free and highly sensitive electrical detection of DNA hybridization, Nano Res. 8 (2015) 2340–2350.

[30] L. Wang, Y. Wang, J.I. Wong, T. Palacios, J. Kong, H.Y. Yang, Functionalized MoS$_2$ nanosheet-based field-effect biosensor for label-free sensitive detection of cancer marker proteins in solution, Small 10 (2014) 1101–1105.

[31] L. Filipovic, S. Selberherr, Gas sensing with two-dimensional materials beyond graphene, in: Proceedings of the 2021 IEEE 32nd International Conference on Microelectronics, (MIEL), 2021, pp. 29–36.

[32] S. Sang, Y. Wang, Q. Feng, Y. Wei, J. Ji, W. Zhang, Progress of new label-free techniques for biosensors: a review, Crit. Rev. Biotechnol. 36 (2016) 465–481.

[33] M. Sedki, Y. Shen, A. Mulchandani, Nano-FET-enabled biosensors: materials perspective and recent advances in North America, Biosens. Bioelectron. 176 (2021), 112941.

[34] W. Shao, S.C. Burkert, D.L. White, V.L. Scott, J. Ding, Z. Li, J. Ouyang, F. Lapointe, P.R. Malenfant, K. Islam, Probing Ca^{2+}-induced conformational change of calmodulin with gold nanoparticle-decorated single-walled carbon nanotube field-effect transistors, Nanoscale 11 (2019) 13397–13406.

[35] D.P. Tran, T.T.T. Pham, B. Wolfrum, A. Offenhäusser, B. Thierry, CMOS-compatible silicon nanowire field-effect transistor biosensor: technology development toward commercialization, Materials 11 (2018) 785.

[36] J. Lee, P. Dak, Y. Lee, H. Park, W. Choi, M.A. Alam, S. Kim, Two-dimensional layered MoS_2 biosensors enable highly sensitive detection of biomolecules, Sci. Rep. 4 (2014) 7352.

[37] H. Nam, B.-R. Oh, P. Chen, J.S. Yoon, S. Wi, M. Chen, K. Kurabayashi, X. Liang, Two different device physics principles for operating MoS_2 transistor biosensors with femtomolar-level detection limits, Appl. Phys. Lett. 107 (2015), 012105.

[38] H. Park, H. Lee, S.H. Jeong, E. Lee, W. Lee, N. Liu, D.S. Yoon, S. Kim, S.W. Lee, $MoS2$ field-effect transistor-amyloid-$\beta1$–42 hybrid device for signal amplified detection of MMP-9, Anal. Chem. 91 (2019) 8252–8258.

[39] Y. Zhang, W. Jiang, D. Feng, C. Wang, Y. Xu, Y. Shan, J. Wang, Z. Yin, H. Deng, X. Mi, Bio-separated and gate-free 2D MoS_2 biosensor array for ultrasensitive detection of BRCA1, Nanomaterials 11 (2021) 545.

[40] L. Daukiya, J. Seibel, S. De Feyter, Chemical modification of 2D materials using molecules and assemblies of molecules, Adv. Phys. X 4 (2019), 1625723.

[41] C.H. Naylor, N.J. Kybert, C. Schneier, J. Xi, G. Romero, J.G. Saven, R. Liu, A. C. Johnson, Scalable production of molybdenum disulfide based biosensors, ACS Nano 10 (2016) 6173–6179.

[42] J. Azadmanjiri, P. Kumar, V.K. Srivastava, Z. Sofer, Surface functionalization of 2D transition metal oxides and dichalcogenides via covalent and non-covalent bonding for sustainable energy and biomedical applications, ACS Appl. Nano Mater. 3 (2020) 3143–3143.

[43] T. Alava, J.A. Mann, C.c. Théodore, J.J. Benitez, W.R. Dichtel, J.M. Parpia, H. G. Craighead, Control of the graphene–protein interface is required to preserve adsorbed protein function, Anal. Chem. 85 (2013) 2754–2759.

[44] S.S. Chou, M. De, J. Kim, S. Byun, C. Dykstra, J. Yu, J. Huang, V.P. Dravid, Ligand conjugation of chemically exfoliated MoS_2, J. Am. Chem. Soc. 135 (2013) 4584–4587.

[45] J.-S. Kim, H.-W. Yoo, H.O. Choi, H.-T. Jung, Tunable volatile organic compounds sensor by using thiolated ligand conjugation on MoS_2, Nano Lett. 14 (2014) 5941–5947.

[46] T. Moehl, M. Abd El Halim, H. Tributsch, Photoelectrochemical studies on the N-MoS_2-cysteine interaction, J. Appl. Electrochem. 36 (2006) 1341–1346.

[47] D. Kong, H. Wang, J.J. Cha, M. Pasta, K.J. Koski, J. Yao, Y. Cui, Synthesis of MoS_2 and $MoSe_2$ films with vertically aligned layers, Nano Lett. 13 (2013) 1341–1347.

[48] L.B. Huang, L. Zhao, Y. Zhang, Y.Y. Chen, Q.H. Zhang, H. Luo, X. Zhang, T. Tang, L. Gu, J.S. Hu, Self-limited on-site conversion of MoO_3 nanodots into vertically aligned ultrasmall monolayer MoS_2 for efficient hydrogen evolution, Adv. Energy Mater. 8 (2018) 1800734.

[49] S.-Y. Cho, S.J. Kim, Y. Lee, J.-S. Kim, W.-B. Jung, H.-W. Yoo, J. Kim, H.-T. Jung, Highly enhanced gas adsorption properties in vertically aligned MoS_2 layers, ACS Nano 9 (2015) 9314–9321.

[50] Y. Wu, H. Fu, A. Roy, P. Song, Y. Lin, O. Kizilkaya, J. Xu, Facile one-pot synthesis of 3D graphite–SiO_2 composite foam for negative resistance devices, RSC Adv. 7 (2017) 41812–41818.

[51] X. Wei, C. Liu, H. Qin, Z. Ye, X. Liu, B. Zong, S. Mao, Fast, specific, and ultrasensitive antibiotic residue detection by monolayer WS_2-based field-effect transistor sensor, J. Hazard Mater. 443 (2023), 130299.

[52] X. Chen, Y. Liu, X. Fang, Z. Li, H. Pu, J. Chang, S. Mao, Ultratrace antibiotic sensing using aptamer/graphene-based field-effect transistors, Biosens. Bioelectron. 126 (2019) 664–671.

[53] R.J. Chen, H.C. Choi, S. Bangsaruntip, E. Yenilmez, X. Tang, Q. Wang, Y.-L. Chang, H. Dai, An investigation of the mechanisms of electronic sensing of protein adsorption on carbon nanotube devices, J. Am. Chem. Soc. 126 (2004) 1563–1568.

[54] M.M. Ali, J.J. Mitchell, G. Burwell, K. Rejnhard, C.A. Jenkins, E. Daghigh Ahmadi, S. Sharma, O.J. Guy, Application of molecular vapour deposited Al_2O_3 for graphene-based biosensor passivation and improvements in graphene device homogeneity, Nanomaterials 11 (2021) 2121.

[55] H. Park, G. Han, S.W. Lee, H. Lee, S.H. Jeong, M. Naqi, A. AlMutairi, Y.J. Kim, J. Lee, W.-j. Kim, Label-free and recalibrated multilayer MoS_2 biosensor for point-of-care diagnostics, ACS Appl. Mater. Interfaces 9 (2017) 43490–43497.

[56] Y.W. Chen, M. Liu, T. Kaneko, P.C. McIntyre, Atomic layer deposited hafnium oxide gate dielectrics for charge-based biosensors, Electrochem. Solid State Lett. 13 (2010) G29.

[57] B.R. Dorvel, B. Reddy Jr., J. Go, C. Duarte Guevara, E. Salm, M.A. Alam, R. Bashir, Silicon nanowires with high-k hafnium oxide dielectrics for sensitive detection of small nucleic acid oligomers, ACS Nano 6 (2012) 6150–6164.

[58] Y. Nakashima, Y. Ohno, S. Kishimoto, M. Okochi, H. Honda, T. Mizutani, Fabrication process of carbon nanotube field effect transistors using atomic layer deposition passivation for biosensors, J. Nanosci. Nanotechnol. 10 (2010) 3805–3809.

[59] R. Niimi, R. Negishi, M. Arifuku, N. Kiyoyanagi, T. Yamaguchi, K. Ishibashi, Y. Kobayashi, Effect of a protective layer on a carbon nanotube thin film channel in a biosensor device, Jpn. J. Appl. Phys. 58 (2019) SIIB14.

[60] J. Rasson, L.A. Francis, Improved stability of porous silicon in aqueous media via atomic layer deposition of oxides, J. Phys. Chem. C 122 (2018) 331–338.

[61] S. Kim, T. Rim, K. Kim, U. Lee, E. Baek, H. Lee, C.-K. Baek, M. Meyyappan, M. J. Deen, J.-S. Lee, Silicon nanowire ion sensitive field effect transistor with integrated Ag/AgCl electrode: PH sensing and noise characteristics, Analyst 136 (2011) 5012–5016.

[62] H. Liu, S.L. Wong, D. Chi, CVD growth of MoS_2-based two-dimensional materials, Chem. Vap. Depos. 21 (2015) 241–259.

[63] Y.H. Lee, X.Q. Zhang, W. Zhang, M.T. Chang, C.T. Lin, K.D. Chang, Y.C. Yu, J.T. W. Wang, C.S. Chang, L.J. Li, Synthesis of large-area MoS_2 atomic layers with chemical vapor deposition, Adv. Mater. 24 (2012) 2320–2325.

[64] Y. Ohno, S. Okamoto, K. Maehashi, K. Matsumoto, Direct electrical detection of DNA hybridization based on electrolyte-gated graphene field-effect transistor, Jpn. J. Appl. Phys. 52 (2013), 110107.

[65] J. Stettner, P. Frank, T. Griesser, G. Trimmel, R. Schennach, E. Gilli, A. Winkler, A study on the formation and thermal stability of 11-MUA SAMs on Au (111)/Mica and on polycrystalline gold foils, Langmuir 25 (2009) 1427–1433.

[66] S. Xu, J. Zhan, B. Man, S. Jiang, W. Yue, S. Gao, C. Guo, H. Liu, Z. Li, J. Wang, Real-time reliable determination of binding kinetics of DNA hybridization using a multi-channel graphene biosensor, Nat. Commun. 8 (2017) 1–10.

[67] M. Bollinger, K.W. Jacobsen, J.K. Nørskov, Atomic and electronic structure of MoS_2 nanoparticles, Phys. Rev. B 67 (2003), 085410.

[68] J.V. Lauritsen, J. Kibsgaard, S. Helveg, H. Topsøe, B.S. Clausen, E. Lægsgaard, F. Besenbacher, Size-dependent structure of MoS_2 nanocrystals, Nat. Nanotechnol. 2 (2007) 53–58.

[69] L.F. Seivane, H. Barron, S. Botti, M.A.L. Marques, Á. Rubio, X. López-Lozano, Atomic and electronic properties of quasi-one-dimensional MoS_2 nanowires, J. Mater. Res. 28 (2013) 240.

[70] S. Mao, G. Lu, K. Yu, Z. Bo, J. Chen, Specific protein detection using thermally reduced graphene oxide sheet decorated with gold nanoparticle-antibody conjugates, Adv. Mater. 22 (2010) 3521–3526.

[71] S. Mao, K. Yu, J. Chang, D.A. Steeber, L.E. Ocola, J. Chen, Direct growth of vertically-oriented graphene for field-effect transistor biosensor, Sci. Rep. 3 (2013) 1–6.

[72] A. Star, J.-C.P. Gabriel, K. Bradley, G. Grüner, Electronic detection of specific protein binding using nanotube FET devices, Nano Lett. 3 (2003) 459–463.

[73] D.A. Healy, C.J. Hayes, P. Leonard, L. McKenna, R. O'Kennedy, Biosensor developments: application to prostate-specific antigen detection, Trends Biotechnol. 25 (2007) 125–131.

[74] C. Hu, I. Zeimpekis, K. Sun, S. Anderson, P. Ashburn, H. Morgan, Low-cost nanoribbon sensors for protein analysis in human serum using a miniature bead-based enzyme-linked immunosorbent assay, Anal. Chem. 88 (2016) 4872–4878.

[75] E. Stern, R. Wagner, F.J. Sigworth, R. Breaker, T.M. Fahmy, M.A. Reed, Importance of the debye screening length on nanowire field effect transistor sensors, Nano Lett. 7 (2007) 3405–3409.

[76] G. Xu, J. Abbott, L. Qin, K.Y. Yeung, Y. Song, H. Yoon, J. Kong, D. Ham, Electrophoretic and field-effect graphene for all-electrical DNA array technology, Nat. Commun. 5 (2014) 1–9.

[77] abcam. ab264615 human PSA ELISA kit. Available online: https://www.abcam.com/human-psa-elisa-kit-ab264615.html (accessed on August, 2022).